

inSIDious Matter

Lucas Durand¹ and Supervised by Sean Tulin¹

¹*Department of Physics and Astronomy, York University, Canada*

Contents

1	Introduction	2
2	Background	2
3	Theory of inSIDious Matter	3
3.1	Quantities of Interest	3
3.2	Feynman Diagrams	4
4	Partial Waves Scattering Theory	4
4.1	1-state scattering (elastic)	4
4.2	2-state scattering (inelastic)	5
5	Numerical Methods	6
5.1	Scattering Quantities	6
5.2	Change of variables	8
5.3	Convergence Requirements	8
5.4	Agreement with previous analytics	9
5.4.1	Born	10
5.4.2	$\delta = 0$	10
6	Analytic Solutions	11
6.1	$d \ll a$	12
6.1.1	Quasi-classical regime	13
6.2	$d \gg a$	14
7	Analysis	15
7.1	Subhalo Structure	15
7.2	Up-scattering Rates	16
7.2.1	Dwarf Scale	16
7.2.2	Cluster Scale	20
7.3	3.56 keV mass-splitting	20
8	Conclusion	22

1 Introduction

In recent years, a number of factors have guided a shift in Dark Matter candidate particle theories from the strong hold of the Cold Collisionless Dark Matter (CCDM) camp to a renewed interest in a DM particle theory characterized by Self-Interactions (SIDM) [5] with a non-trivial velocity dependence [6]. The close study of Milky Way (MW) dwarf spheroidal (dSph) satellite galaxies as well as the Bullet Cluster has produced a wealth of data pertaining to DM halo structures. The relatively high mass:light ratio in dSph galaxies make them an ideal laboratory [7] for investigating the dark sector, while the kinematics of the Bullet Cluster collision provides hard constraints [8] on a SIDM theory. These observations, in conjunction with N-body simulations [9–11] of CCDM, provide the basis for the move from CCDM into SIDM. The added observations of the yet-unexplained 3.56 keV x-ray emission line observationseSS38,SS39 emanating from a large stack of galactic clusters further support the consideration of possibility of SIDM scattering inelastically into an excited state, whose decay is responsible for this and possibly other line emission events. For the 3.56 keV emission in particular, the ruling out of DM annihilation [33] as its cause further points to the explanatory potential of an inelastic self-interacting dark matter (inSIDious Matter) theory. Here we first present a brief background of the motivation behind the re-emergence of SIDM-type theories for DM, then branch off from the typical 1-state SIDM [1] to develop the framework to analyse a simple inelastic dark matter candidate [3], where we aim to extend the analysis beyond purely an s-wave treatment to determine parameter space restrictions from both halo structure and line emission events.

2 Background

The issues arising from CCDM that motivated this move can be summarized as three central problems [1]. The first is the missing satellites problem [14, 15]. This issue centres around a discrepancy between observed MW satellites and predicted MW satellites according to CCDM N-body simulations which predict a much larger number of MW satellites than have yet been detected. The nature of CCDM allows for a dense and complicated DM halo structure with the formation of substructures and subsubstructures. This issue can be addressed by the addition of self interactions to the DM model, moving to a SIDM model. This move suppresses the halo mass function at small scales and reduces the number of predicted MW satellites.

Secondly, there is the core-vs-cusp problem. N-body simulations of CCDM [21–23] predict a mass-density distribution featuring a severely cuspy centre. This is directly contradicted by observations of dwarf galaxies which feature a prominent core [20, 24–27] of relatively constant density. A solution to this problem is the introduction of a self-interaction for DM particles characteristic of a SIDM theory. By maintaining an appropriate lower bound [9–11] on the self-interaction cross-section of DM particles, a mechanism is created for higher energy outer-halo DM particles to transfer energy to inner-halo particles, knocking them out of a central position and flattening the cusp into the observationally consistent core until the halo structure settles into a cored thermal equilibrium [7].

Finally, the too-big-to-fail problem arises from the fact that the most massive subhalos in

CCDM simulations are both too massive and having too large a central density to host the brightest observed satellites [14, 15, 28]. CCDM simulations predict subhalos with a circular velocity too large to explain dSph observations and rule out the idea that the most massive subhalos give rise to the brightest satellites [29]. This issue as a whole can be dealt with through a DM model that predicts lower central density and subhalo mass structure, both of which are consistent with SIDM.

3 Theory of inSIDious Matter

The move to inSIDious Matter from SIDM is motivated strongly by the eXciting Dark Matter mechanism outlined in [2]. In this case we will consider a model with an interaction Lagrangian

$$\mathcal{L}_{\text{int}} = g_X \bar{X}_j X_i \vec{\phi} + \frac{1}{m_X} X_2 \sigma^{\mu\nu} X_1 F_{\mu\nu} \quad (1)$$

for $j \neq i$ with the dark fine structure constant $\alpha_X = g_X^2/(4\pi)$ and the second term, the dipole operator, mediating a decay from an excited state to the ground state of the form $X_2 \rightarrow X_1 \gamma$, where we take the mass-splitting between a ground and excited state, δ , to result in the emission of a photon, γ , of energy δ . This model also includes a decay mechanism for $X_2 \rightarrow X_1 e^+ e^-$ which is inaccessible for $\delta < 2m_e$ where γ -decay is the only decay mechanism. Although this mechanism will not receive a direct treatment in this paper, the ability to supplement the results of the model with the possibility to explain excess positron emissions detected by INTEGRAL/SPI [30–32] further bolsters the efficacy of the theory.

3.1 Quantities of Interest

By assuming that DM particles in the excited state immediately decay as Xray emission and that the mass-splitting is sufficiently small to negate dissipation, a typical halo structure would be effected only by the momentum transfers of collisions of ground-state DM. We know that the total momentum transfer cross-section has a hard limit determined by N-body simulations [9–11], observations of the Bullet Cluster [8], and recent analysis of surveys of galaxies [7] of

$$\frac{\sigma_{\text{dwarf}}^T}{m_X} \sim 1 \frac{cm^2}{g} \quad \frac{\sigma_{\text{cluster}}^T}{m_X} \sim 0.1 \frac{cm^2}{g} \quad (2)$$

where the momentum transfer cross-sections are defined as $\sigma^T = \int \frac{d\sigma}{d\Omega} (1 - \cos \theta) d\Omega$ and are a quantity which lends itself quite well to plasma-type physics and analysis of halo structure and substructure.

We are only interested in the momentum transfer cross-sections for processes in which the DM is initially in the ground-state (as depicted in §3.2), so we seek $\sigma_{fi}^T = \sigma_{f1}^T$. In particular we want to find the total momentum-transfer cross-section, $\sigma_{11}^T + \sigma_{21}^T$ and the upscattering rate, σ_{21} , where the upscattering rate is an unweighted cross-section.

3.2 Feynman Diagrams

Here we attach the Feynman diagrams for the relevant processes outlined in §3.1. The two major scattering processes of interest, the ground-state scattering and upscattering are facilitated by the exchange of the dark boson ϕ under the dark Yukawa force. The ground-state ($|11\rangle \rightarrow |11\rangle$) scattering requires two force exchanges, as, at tree level, the ground-state DM particle actually upscatters momentarily into an X_2 state before downscattering back to the ground-state.

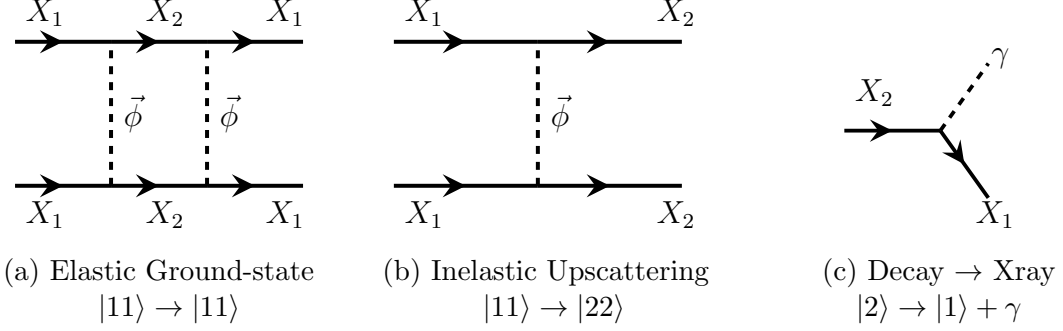


Figure 1: Scattering Processes

4 Partial Waves Scattering Theory

Now we are ready to move forward in setting up the scattering problem and (eventually) calculating the characteristic cross-sections. First, we outline the traditional approach for elastic scattering using a partial waves expansion which decouples the problem into angular momentum modes, ℓ , then we develop a numerical method for solving the Schrödinger equation for an inelastic exchange.

4.1 1-state scattering (elastic)

We write the total wave function in its familiar form as the sum of an incoming plane wave and outgoing scattered state wavefunction.

$$\Psi(r) = ce^{ikz} + f(\theta) \frac{e^{ikr}}{r} \quad (3)$$

In the large limit, we can represent the radial part of this wavefunction as

$$R_\ell \xrightarrow{r \gg 0} c_\ell^{(1)} \underbrace{h_\ell^{(1)}(kr)}_{\text{outgoing}} + c_\ell^{(2)} \underbrace{h_\ell^{(2)}(kr)}_{\text{incoming}} \quad (4)$$

Given that the Hankel functions behave asymptotically as

$$h_\ell^{(1)}(kr) \xrightarrow{r \rightarrow \infty} \frac{i^{-\ell}}{ik} \frac{e^{ikr}}{r} \quad h_\ell^{(2)}(kr) \xrightarrow{r \rightarrow \infty} \frac{-i^\ell}{ik} \frac{e^{-ikr}}{r} \quad (5)$$

we can rewrite the wavefunction in the form of Eq. (3) by separating the incoming plane wave from the outgoing part of the radial wavefunction.

$$R_\ell \xrightarrow{r \gg 0} \left(c_\ell^{(1)} - c_\ell^{(2)} \right) h_\ell^{(1)}(kr) + c_\ell^{(2)} \left(h_\ell^{(1)}(kr) + h_\ell^{(2)}(kr) \right) \quad (6)$$

As we can write the total wavefunction with the choice of an overall coefficient A_ℓ , we use

$$\Psi_\ell = P_\ell(\cos \theta) R_\ell A_\ell \quad A_\ell = i^\ell \frac{(2\ell + 1)}{2} \quad (7)$$

Which when taken to the asymptotic limit yields

$$\Psi \xrightarrow{r \rightarrow \infty} \sum_\ell c_\ell^{(2)} P_\ell(\cos \theta) (2\ell + 1) \left(\frac{e^{ikr}}{2ikr} - (-1)^\ell \frac{e^{-ikr}}{2ikr} \right) + \sum_\ell P_\ell(\cos \theta) \frac{(2\ell + 1)}{2ik} \left(c_\ell^{(1)} - c_\ell^{(2)} \right) \frac{e^{ikr}}{r} \quad (8)$$

$$= ce^{ikz} + \underbrace{\sum_\ell P_\ell(\cos \theta) \frac{(2\ell + 1)}{2ik} \left(c_\ell^{(1)} - c_\ell^{(2)} \right) \frac{e^{ikr}}{r}}_{f_\ell(\theta)} \quad (9)$$

Thus we have found the sought-after scattering amplitude for a particular wavefunction in terms of the Hankel function coefficients in the large limit.

4.2 2-state scattering (inelastic)

Now we can proceed by solving the relevant radial S.E. for two particle inelastic scattering

$$\frac{d}{dr} \left(r^2 \frac{d\vec{R}_\ell(r)}{dr} \right) - m_\chi r^2 (\mathcal{V}(r) - m_\chi v^2) \vec{R}_\ell(r) = \ell(\ell + 1) \vec{R}_\ell(r) \quad (10)$$

where the scattering potential is defined by $\mathcal{V}(r) = \begin{pmatrix} 0 & V(r) \\ V(r) & 2\delta \end{pmatrix}$, $V(r) \equiv -\alpha_\chi \frac{e^{-m_\phi r}}{r}$ for a small mass gap between states of δ , a dark matter mass $m_\chi = 2\mu$, a dark mediator mass of m_ϕ , dark fine structure constant α_χ and DM velocity in the centre-of-mass frame, $v = v_{\text{rel}}/2$. Given the 2×2 -matrix form of the scattering potential, we will require a 2×2 -coefficient matrix for initial states, which in the small r limit we can represent as

$$R_\ell^{ij}(r \approx 0) = \mathcal{C}^{ij} r^\ell \quad (11)$$

Accordingly we will need to promote the radial wavefunctions from §4.1 into a matrix form. We now are dealing with a radial wavefunction which behaves as

$$R_\ell^{ij} \xrightarrow{r \gg 0} c_{\ell[i,j]}^{(1)} \underbrace{h_\ell^{(1)}(k_i r)}_{\text{outgoing}} + c_{\ell[i,j]}^{(2)} \underbrace{h_\ell^{(2)}(k_i r)}_{\text{incoming}} \quad (12)$$

If we are to move forward as intended, we will be evolving the S.E. from small to large r and determining the characteristic Hankel coefficients $c_{\ell[i,j]}^{(1)}, c_{\ell[i,j]}^{(2)}$ by matching onto the large-valued solution at some yet-to-be-determined large-enough point r_m . As it stands, we will find a solution of the form

$$\Psi = e^{i[K]z} \left((\vec{c}_1)(\vec{c}_j) \right) + \frac{e^{i[K]r}}{r} [F] \quad (13)$$

where $[C] = \begin{pmatrix} (\vec{c}_1)(\vec{c}_j) \end{pmatrix}$ has columns of the incoming states at the asymptotic limit, \vec{c}_j , $[K] = \begin{pmatrix} k_1 & 0 \\ 0 & k_2 \end{pmatrix}$, and $[F]^{ij} = f^{nj}$ is the scattering amplitude matrix, quantifying the transitions $|jj\rangle \rightarrow |nn\rangle$ which correspond to an incoming state of amplitude \vec{c}_j scattering to a state with amplitude \vec{c}_n .

5 Numerical Methods

The most physically interesting case will be for $[C] = \mathbb{1}$, meaning we will have mass-distinct states scattering into mass-distinct states (e.g. $|11\rangle \rightarrow |11\rangle, |11\rangle \rightarrow |22\rangle, \dots$) Because we wish to set the initial conditions for small r and evolve the S.E. into the asymptotic limit, we must choose appropriate relative initial amplitudes so that the incoming plane wave scales with unity, meaning $R_\ell \rightarrow \dots + \mathbb{1} h_\ell^{(2)}$ or $c_\ell^{(2)} = \mathbb{1}$. We can do this by first evolving the S.E. with arbitrary initial conditions and rotating the resultant matrix equation into the mass-eigenstate frame. If we choose to write the plane wave coefficient matrix as some unitary matrix $c_\ell^{(2)} = \mathcal{U}_\ell$, we can achieve the desired rotation simply by applying the matrix inverse across the equation.

We can write the rotated R.S.E. as

$$\mathcal{R}_\ell^{ij}(r) = R_\ell^{ik}(r) (\mathcal{U}_\ell^{-1})_{kj} \quad (14)$$

which at some large matching point r_m will go to

$$\mathcal{R}_\ell^{ij}(r_m) = c_{\ell[i,k]}^{(1)} (\mathcal{U}_\ell^{-1})_{kj} h_\ell^{(1)}(k_i r_m) + \mathbb{1}_{ij} h^{(2)}(k_i r_m) \quad (15)$$

It now suffices to determine the coefficients $c^{(1)}, c^{(2)}$ at the matching point r_m from the system of equations

$$\begin{cases} R_\ell^{ij}(r_m) = h_\ell^{(1)}(\vec{k}_i r_m) c_{\ell[i,j]}^{(1)} + h_\ell^{(2)}(\vec{k}_i r_m) c_{\ell[i,j]}^{(2)} \\ R'_\ell^{ij}(r_m) = \underbrace{k \left(\frac{1}{2} \left(h_{l-1}^{(1)}(k x_m) - h_{l+1}^{(1)}(k x_m) \right) - \frac{h_l^{(1)}(k x_m)}{2 k x_m} \right)}_{h'^{(2)}} c_{\ell[i,j]}^{(1)} + \underbrace{\frac{1}{2} \left(h_{\ell-1}^{(2)}(\vec{k}_i r_m) - h_{\ell+1}^{(2)}(\vec{k}_i r_m) \right)}_{h'^{(2)}} c_{\ell[i,j]}^{(2)} \end{cases} \quad (16)$$

which reduces to

$$c_{\ell[i,j]}^{(1)} = -\frac{R_\ell^{ij}(r_m) h'^{(2)}(k_i r_m) - h_\ell^{(2)}(k_i r_m) R'_\ell^{ij}(r_m)}{h_\ell^{(2)}(k_i r_m) h'^{(1)}(k_i r_m) - h_\ell^{(1)}(k_i r_m) h'^{(2)}(k_i r_m)} \quad (17)$$

$$c_{\ell[i,j]}^{(2)} = -\frac{-R_\ell^{ij}(r_m) h'^{(1)}(k_i r_m) + h_\ell^{(1)}(k_i r_m) R'_\ell^{ij}(r_m)}{h_\ell^{(2)}(k_i r_m) h'^{(1)}(k_i r_m) - h_\ell^{(1)}(k_i r_m) h'^{(2)}(k_i r_m)} \quad (18)$$

5.1 Scattering Quantities

We can now read off the scattering amplitude from Eq. (15), taking on an overall factor of $1/ik_i$ to account for the discrepancy between the asymptotic Hankel functions in Eq. (5) and

the desired outgoing spherical wave in Eq. (9)

$$f_\ell^{ij} = \frac{1}{ik_i} \left(c_{\ell[i,k]}^{(1)} (\mathcal{U}_\ell^{-1})_{kj} - \mathbb{1}_{ij} \right) \quad (19)$$

with the angular dependence,

$$f^{ij}(\theta) = \sum_{\ell}^{\ell_{\max}} P_\ell(\cos \theta) A_\ell f_\ell^{ij} \quad (20)$$

and accordingly the differential cross-section

$$\frac{d\sigma^{ij}}{d\Omega} = \frac{k_i}{k_j} |f^{ij}(\theta)|^2 = \frac{1}{4k_i k_j} \left| \sum_{\ell}^{\ell_{\max}} P_\ell(\cos \theta) i^{\ell-1} (2\ell+1) \left(c_{\ell[i,k]}^{(1)} (\mathcal{U}_\ell^{-1})_{kj} - \mathbb{1} \right) \right|^2 \quad (21)$$

from here we are interested in three cross-sectional quantities, the purely rate cross-section,

$$\sigma^{ij} = \int_{\Omega} \frac{d\sigma^{ij}}{d\Omega} \sin \theta d\theta d\phi \quad (22)$$

which will be used for some numerical checks, the partial momentum transfer cross-section,

$$\sigma_{T/rate}^{ij} = \int_{\Omega} \frac{d\sigma^{ij}}{d\Omega} (1 - \delta_{ij} \cos \theta) \sin \theta d\theta d\phi \quad (23)$$

weighted only in the matrix elements corresponding to self-scattering, which suppresses the $|11\rangle \rightarrow |11\rangle$ term, allowing easier convergence and extraction of upscattering information $|11\rangle \rightarrow |22\rangle$, and the total transfer cross-section,

$$\sigma_T^{ij} = \int_{\Omega} \frac{d\sigma^{ij}}{d\Omega} (1 - \cos \theta) \sin \theta d\theta d\phi \quad (24)$$

which will give us information pertaining to halo structure. We can decouple Eq. (23) into an analytic result by noting the Legendre orthogonality relations

$$\begin{aligned} \int_0^\pi P_\ell(\cos \theta) P_m(\cos \theta) \sin \theta d\theta &= \frac{2\delta_{\ell m}}{2\ell + 1} \quad \int_0^\pi P_\ell(\cos \theta) P_m(\cos \theta) \cos \theta \sin \theta d\theta = \frac{2(\ell + 1)\delta_{(\ell+1)m}}{(2\ell + 1)(2\ell + 3)} \\ \sigma_{T/rate} &= \pi \sum_{\ell}^{\infty} \left(\underbrace{(2\ell + 1) |f_\ell|^2}_{\sigma_{\text{total}}} - \underbrace{2(\ell + 1) |f_\ell f_{\ell+1}| \circ \mathbb{1}}_{\sigma_{\text{weighted on diagonal}}} \right) \end{aligned} \quad (25)$$

From this equation it is simple to formulate the purely rate cross-section or the total transfer cross-section by taking $\mathbb{1} \rightarrow 0/1$ respectively

5.2 Change of variables

We write the radial wavefunction in terms of the function $\vec{\chi}_\ell(r) = r \vec{R}_\ell(r)$, by making note of the relationship $\frac{1}{r} \frac{d}{dr} (r^2 \frac{d}{dr} R_\ell(r)) = \frac{d^2}{dr^2} (r R_\ell(r))$

$$\left(\frac{d^2}{dr^2} + m_\chi^2 v^2 - \frac{\ell(\ell+1)}{r^2} - m_\chi \mathcal{V}(r) \right) \vec{\chi}_\ell(r) = 0 \quad (26)$$

we can determine the momentum by looking at the large limit (in which the centrifugal potential vanishes) where $k_j = \sqrt{m_\chi^2 v^2 - m_\chi \mathcal{V}_{jj}(\infty)}$ and with the additional introduction of

$$x = \alpha_\chi m_\chi r \quad a = \frac{v}{\alpha_x} \quad b = \frac{\alpha_\chi m_\chi}{m_\phi} \quad d = \sqrt{\frac{2\delta}{m_\chi \alpha_\chi^2}} \quad (27)$$

the differential equation of question can be compactly written, with $V(r)$ as in §4.2

$$\chi''(r) = \begin{pmatrix} \frac{\ell(\ell+1)}{r^2} - a^2 & V(r) \\ V(r) & \frac{\ell(\ell+1)}{r^2} - a^2 + d^2 \end{pmatrix} \chi(r) \quad (28)$$

Finally, in order to solve for the asymptotic coefficients in Eq. (17), Eq. (18), we rewrite $k_j r \rightarrow \sqrt{a^2 - \delta_{j2} d^2} x$ and transform the system in Eq. (16) to

$$\begin{cases} \chi_\ell^{ij}(x_m) = x_m h_l^{(1)}(k_i x_m) c_{\ell[i,j]}^{(1)} + x_m h_l^{(2)}(k_i x_m) c_{\ell[i,j]}^{(2)} \\ \chi'_\ell^{ij}(x_m) = c_1 h_l^{(1)}(k_i x_m) + c_1 k x_m \left(\frac{1}{2} \left(h_{l-1}^{(1)}(k_i x_m) - h_{l+1}^{(1)}(k_i x_m) \right) - \frac{h_l^{(1)}(k_i x_m)}{2 k_i x_m} \right) + \\ c_2 h_l^{(2)}(k_i x_m) + c_2 k x_m \left(\frac{1}{2} \left(h_{l-1}^{(2)}(k_i x_m) - h_{l+1}^{(2)}(k_i x_m) \right) - \frac{h_l^{(2)}(k_i x_m)}{2 k_i x_m} \right) \end{cases} \quad (29)$$

5.3 Convergence Requirements

The algorithm developed solves the S.E. over increasingly large ranges of $[x_i, x_m]$ until the corresponding scattering amplitudes f_ℓ converge at 1%. This is split into two processes, first increasing the upward matching value x_m until convergence, then decreasing the initial value x_i until a second convergence produces f_ℓ and thereby σ_ℓ^T or σ_ℓ . This process is replicated in solving for the cross-section by requiring that the summation of ℓ modes converges itself at 1%. In some regions this approach runs into difficulties.

Near the Born limit, $b \sim 1$, ℓ -modes outside the s-wave ($\ell = 0$) can sometimes oscillate rapidly without quick convergence. In this case it is safe to take $f_{\ell>0} \rightarrow 0$ if the amplitude is oscillating many orders of magnitude smaller than the previous converged f_ℓ .

Lastly, as we calculate the cross-section in the classical regime ($ab \gtrsim 1$) contributions from higher ℓ -modes become important and typically we will need to sum over many of these modes. With more modes to sum over we sometimes encounter a false convergence. To rectify this, we require 10 successive ℓ -mode convergences, which functionally eliminates this issue.

5.4 Agreement with previous analytics

To compare our numerical results with known benchmarks, we plot $\sigma_1^T(b)$ for a constant velocity ($a_{dw} = v_{dw}/\alpha$). We are interested in confirming both that the numerics approach analytic results in the perturbative regime for small values of b , as well as maintaining the predicted peak structure through the resonant regime ($1 \lesssim b \lesssim 1/a$) and into the classical regime ($ab > 1$). Before jumping into confirming these results, it is useful to qualitatively analyse a typical plot. There is quite a bit of information being represented in Figure 2. The

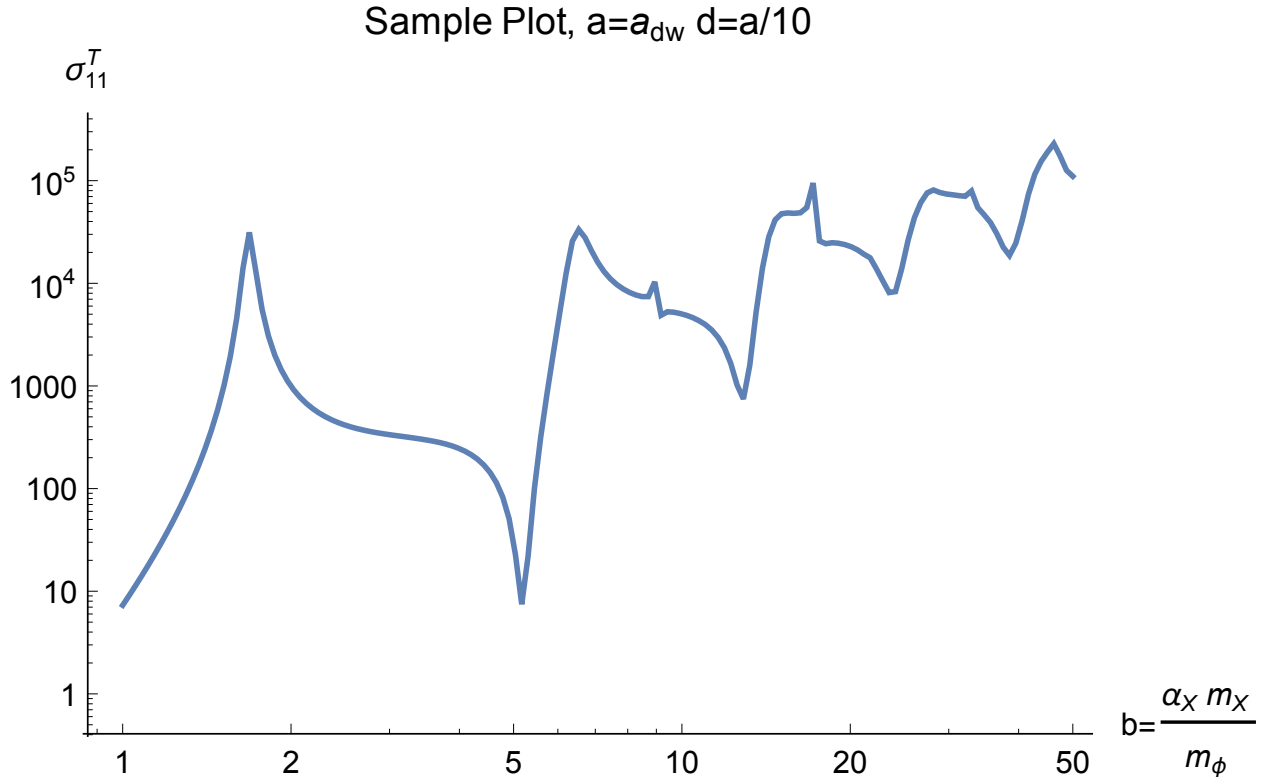


Figure 2: Ground-state elastic transfer cross-section for b -values between the Born limit and the classical regime on the dSph scale, $a_{dw} = 0.01$ with a negligible mass-splitting $d = a_{dw}/10$

domain of the plot spans from the perturbative regime, where b is small, through much of the resonant regime, stopping before b reaches a large enough value to be considered in the classical regime, but suffices to demonstrate the important features in the resonant regime of a typical plot.

At the far left of the plot, we are firmly in the perturbative regime. Here, for low b , the range of the force is relatively small and can be treated as a point interaction, modelled analytically by the Born approximation. Moving from left to right, we see distinctly two large peaks upward and downward respectively, which are the first s-wave ($\ell = 0$) resonance and anti-resonance at $b_{\text{res}} \sim 1.7$ and $b_{\text{anti}} \sim 5$. Continuing to the right we see the alternating pattern of s-wave resonance/anti-resonance becoming less well-defined. This is due to the increasing contributions of higher ℓ -modes to the total cross-section adding onto the base s-wave shape (which is plotted alone in Figure 4). Scanning from left to right we see the first

p-wave ($\ell = 1$) resonances followed shortly by anti-resonances at $b \sim 9$ and further resonances at $b \sim 19, 35$. Moving closer to the classical regime where $ab \sim 1$, the contributions from higher ℓ -modes dominates the total cross-section, and individual resonances are hidden.

5.4.1 Born

We investigate the behaviour of the numerical solution approaching the Born limit $\left(\lim_{a \rightarrow 0} \sigma_T^{11} + \sigma_T^{21}\right)$ for various choices of (b, d) . In terms of dimensionless parameters, the Born approximation for the total ground-state scattering can be written, for $b \lesssim 1$ [3],

$$\sigma_T^{\text{Born}} = \underbrace{\pi b^6 \frac{1}{(1+bd)^4}}_{\sigma_B^{11}} + \underbrace{\frac{\sqrt{d^2 - a^2}}{a} \frac{4\pi b^4}{(1-d^2b^2)^2 + 4a^2b^2}}_{\sigma_B^{21}} \quad (30)$$

In Figure 3, we have plotted the numerical result (σ) and the Born result (σ_B) for small a at a constant value, such that $a \ll b < 1$. As can be seen in Figure 3, the approximation is very accurate, falling within 1% for $a \ll b \lesssim 0.2$, showing that the numerical solution does indeed approach the Born limit. Also of note, the disagreement increases rapidly as $b \rightarrow 1$ and beyond, as the second-order perturbative expansion blows up in comparison to the numerical solution.

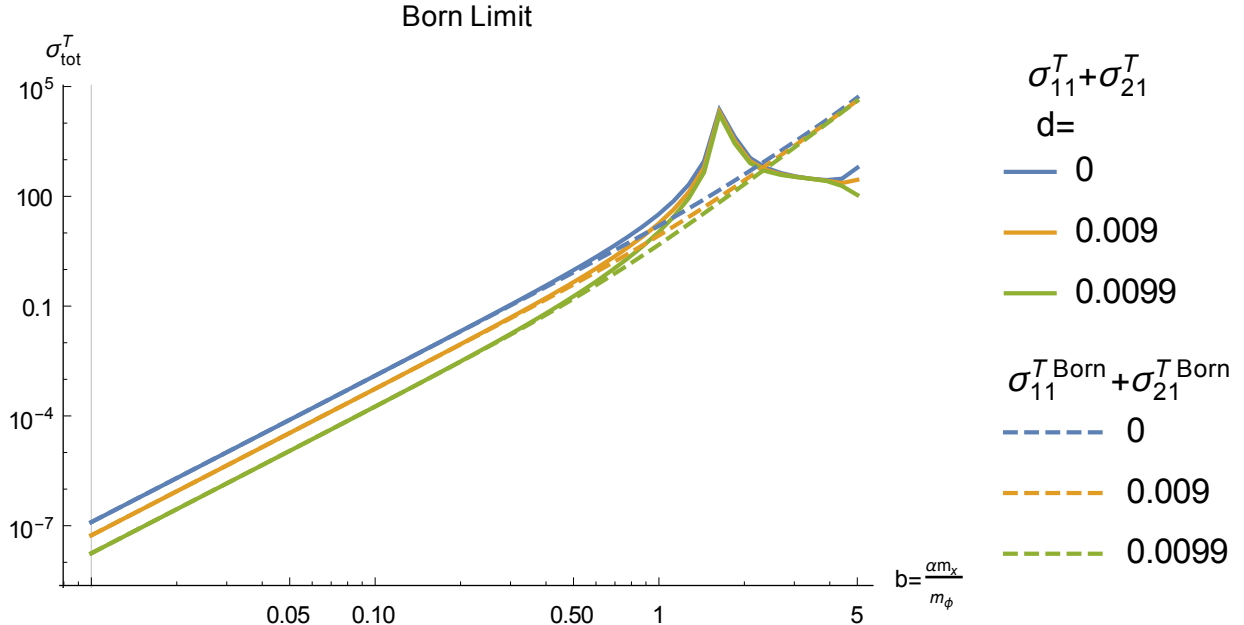


Figure 3: Numerical cross-section and the Born limit for various d -values on the dSph scale, $a = 0.01$

5.4.2 $\delta = 0$

Where there is no mass-splitting, we should be able to recover the results for 1-state scattering. Here we quickly compare the total 2-state numeric s-wave transfer cross-section to

the result using the analytic form of the phase shifts from [1].

For 1-state scattering we can write the s-wave transfer cross-section in terms of the phase shift picked up by the spherical wave far from the scattering centre as compared to a free particle, where we divide by an overall factor of 1/2 to account for the double counting of the now identical ground/excited states,

$$\sigma_T^{11+21} = \frac{1}{2} \frac{4\pi}{k^2} \sum_{\ell} (\ell + 1) \sin^2(\delta_{\ell+1} - \delta_{\ell}) \quad (31)$$

We also make use of the analytic result for the s-wave phase shift [1] which substitutes the Hulthén potential for Yukawa and defines

$$\lambda_{\pm} \equiv \begin{cases} 1 + iac + i\sqrt{c + a^2 c^2} & \text{repulsive} \\ 1 + iac + \sqrt{c - a^2 c^2} & \text{attractive} \end{cases} \quad c \equiv \frac{\alpha_X m_X}{m_\phi(1.6)} \quad (32)$$

to write

$$\delta_0 = \arg \left(\frac{i\Gamma(\lambda_+ + \lambda_- - 2)}{\Gamma(\lambda_+) \Gamma(\lambda_-)} \right) \quad (33)$$

Indeed, our numerics (albeit with much unnecessary effort) are able to reproduce the ana-

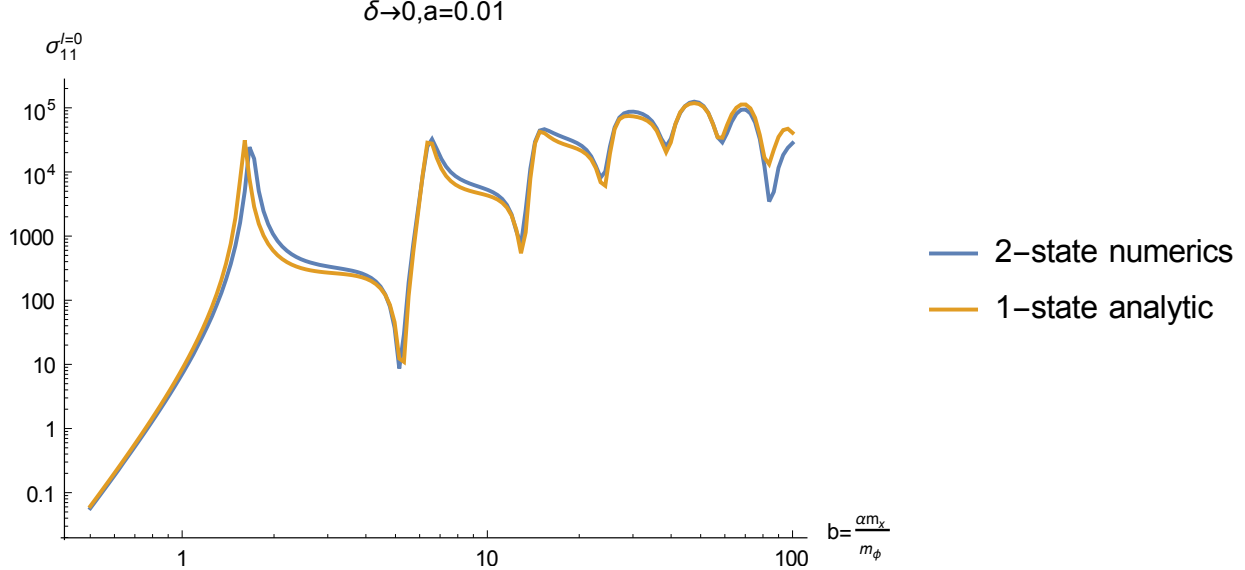


Figure 4: 1-state comparison for $\delta=0$

lytic formula for s-wave scattering (see Figure 4) with close accuracy. In particular the formula agrees well at the s-wave resonances/anti-resonances and follows the numerics tightly between.

6 Analytic Solutions

There are certain regions of interest in which we can make use of some novel analytic solutions in order to reduce computation time.

6.1 $d \ll a$

In this limit the two mass eigenstates are effectively degenerate, meaning that $\delta \rightarrow 0 \implies$ we can decouple the 2-state problem into a 1-state problem decomposed into attractive/repulsive eigenstates and solve using analytic 1-state methods [1]. (N.B. this is what we have used in §5.4.2)

Here we simplify the differential equation by diagonalizing the potential function. We can write $V = U^\dagger \bar{V} U$ and make a coordinate change such that $\chi \rightarrow U^\dagger \eta U$, where we identify U as the unitary matrix of the eigenvectors of V . When we write

$$\chi'' = \left(\left(-a^2 + \frac{\ell(\ell+1)}{x^2} \right) + V \right) \chi \quad (34)$$

we can solve the eigenvalue problem $U = (\xi_1, \xi_2)$ where ξ_1, ξ_2 are normalized eigenvectors of V , to find:

$$U(x) = \begin{pmatrix} \frac{e^{x/b} x d^2 + \sqrt{e^{\frac{2x}{b}} x^2 d^4 + 4}}{\sqrt{\left(e^{x/b} x d^2 + \sqrt{e^{\frac{2x}{b}} x^2 d^4 + 4} \right)^2 + 4}} & \frac{2}{\sqrt{\left(e^{x/b} x d^2 + \sqrt{e^{\frac{2x}{b}} x^2 d^4 + 4} \right)^2 + 4}} \\ \frac{d^2 e^{x/b} x - \sqrt{e^{\frac{2x}{b}} x^2 d^4 + 4}}{\sqrt{\left(\sqrt{e^{\frac{2x}{b}} x^2 d^4 + 4} - d^2 e^{x/b} x \right)^2 + 4}} & \frac{2}{\sqrt{\left(\sqrt{e^{\frac{2x}{b}} x^2 d^4 + 4} - d^2 e^{x/b} x \right)^2 + 4}} \end{pmatrix} \quad (35)$$

Taking $d = 0$,

$$U(x) = U = \frac{1}{\sqrt{2}} \begin{pmatrix} 1 & 1 \\ -1 & 1 \end{pmatrix} \quad U' = [U^\dagger]' = 0 \quad \bar{V}(x) = \frac{e^{-x/b}}{x} \begin{pmatrix} -1 & 0 \\ 0 & 1 \end{pmatrix} \quad (36)$$

which when transformed and acted on from the left by U and the right by U^\dagger , noting $UU^\dagger = U^\dagger U = 1$

$$\eta'' = \left(-a^2 + \frac{\ell(\ell+1)}{x^2} + \bar{V} \right) \eta - \underbrace{f(U', U'', [U^\dagger]', [U^\dagger}'', \eta, \eta')}_{\text{higher-order terms}} \quad (37)$$

We have successfully decoupled the Schrödinger equation and can proceed in solving the system η_{11}, η_{22} and rotating back into the χ basis to recover the off-diagonal terms. Explicitly:

$$\begin{cases} \eta_\ell^{11''} &= \left(-a^2 + \frac{\ell(\ell+1)}{x^2} - \frac{e^{-x/b}}{x} \right) \eta_\ell^{11} \\ \eta_\ell^{22''} &= \left(-a^2 + \frac{\ell(\ell+1)}{x^2} + \frac{e^{-x/b}}{x} \right) \eta_\ell^{22} \end{cases} \quad (38)$$

which when solved numerically agrees perfectly for $d = 0$ with earlier numerical methods (as they are equivalent), and is within $\sim 0.1\%$ for $d < 0.1a \wedge ab \gtrsim 1$.

We can now write down the scattering amplitude for a single-state from the phase shift and promote it to matrix form for decoupled quasi-classical scattering. Absorbing the factor

of $1/2ik$ into the definition of the cross-section and rotating the result back into the coupled state to recover both upscattering and downscattering information

$$f_\ell^\pm = e^{2i\delta_\ell^\pm} - 1 \xrightarrow{\eta \rightarrow \chi} f_\ell = U^\dagger \begin{pmatrix} e^{2i\delta_\ell^+} & 0 \\ 0 & e^{2i\delta_\ell^-} \end{pmatrix} U - 1 \quad (39)$$

which, taking $|f_\ell|$, agrees with numerical solutions using the algorithm developed in §5.2 to $\sim 5\%$ within the classical regime, with a computation time several orders of magnitude fewer.

6.1.1 Quasi-classical regime

In particular, calculations of cross-section are most computationally taxing in the classical regime, characterized by $(ab > 1)$. In this regime, the cross-section is no longer dominated by $\ell = 0$ s-wave contributions and typically picks up a large number of ℓ -modes, each requiring a large number of solutions of the S.E. in order to converge.

By using the method from Landau-Lifshitz (L-L) [4], we can find phase shifts from the numerical evaluation of a simple convergent integral. This approach is accurate for $ab \gg 1$ and $\ell \gg 0$. In particular, the dominant contributions come from the phase shifts for values of ℓ in which the corresponding scattering amplitude $f(\theta)$ is found in extremum, satisfying

$$2 \frac{d\delta_\ell}{d\ell} \pm \theta = 0 \quad (40)$$

In general in the quasi-classical regime, the asymptotic phase shift tends to

$$\delta_\ell = \int_{r_0}^{\infty} \left\{ \frac{1}{\hbar} \sqrt{2m(E - V) - \hbar^2 \frac{(\ell + \frac{1}{2})^2}{r^2}} \right\} dr + \frac{\pi}{2} (\ell + \frac{1}{2}) - kr_0 \quad (41)$$

Inserting the dark Yukawa potential and transforming into the familiar dimensionless coordinates by Eq. (27), the phase shift :

$$[\delta_\ell^\pm]^i = \int_{\ell/k_i}^{\infty} \left\{ \sqrt{(a^2 - \delta_{i2} d^2) \mp \frac{2}{x} e^{-x/b} - \frac{(\ell + \frac{1}{2})^2}{x^2}} - a \right\} dx + \frac{\pi}{2} (\ell + \frac{1}{2}) - \ell \quad (42)$$

For a weakly coupled potential, $\beta = 1/a^2 b \ll 1$ and large values of ℓ we are able to expand and write the phase shift δ_ℓ as in [4] §123,

$$\delta_\ell = - \int_{\ell/k}^{\infty} \frac{m_\chi V(r)}{\hbar^2 \sqrt{k^2 - \frac{(\ell + \frac{1}{2})^2}{r^2}}} dr \quad (43)$$

Inserting the dark Yukawa potential and transforming into the familiar dimensionless coordinates by Eq. (27):

$$[\delta_\ell^\pm]^i = \mp \int_{\ell/k_i}^{\infty} \frac{e^{-x/b}}{\sqrt{(a^2 - \delta_{i2} d^2)x^2 - (\ell + \frac{1}{2})^2}} dx \quad (44)$$

for the attractive(−)/repulsive(+) potential, where included are both the ground and excited state elastic scattering phase shifts. It is worth noting that for large ℓ , the phase shifts from attractive and repulsive potentials are related by $\delta_l^+ = -\delta_l^-$

Comparing values for the phase shift Eq. (44), δ_ℓ^{L-L} , to numerical calculations of δ_ℓ^{S-S} using the `SchrodingerSolver` module [1], there is agreement up to $\approx 5\%$ for $ab \gtrsim 5 \wedge \ell \gtrsim 10$, with deviations approaching 100% for low ℓ and as $ab \lesssim 1$.

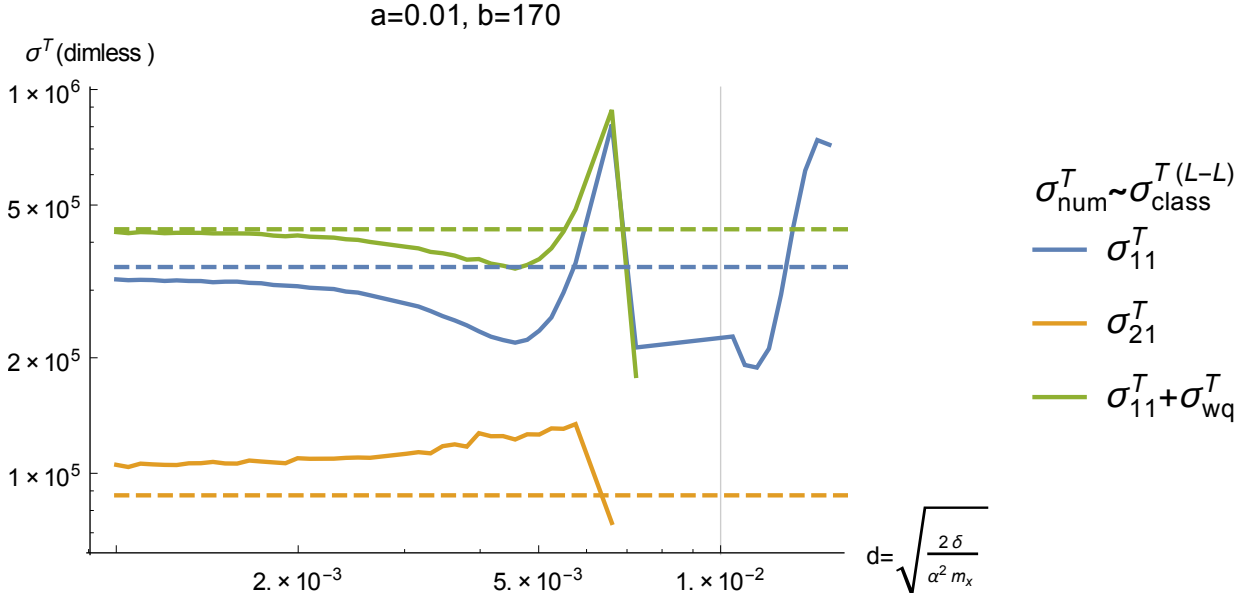


Figure 5: Classical Results. Dashed lines: $\sigma_{T/cl}^{\delta=0}$ classical numerics, Solid lines: numerics

Noticeable in Figure 5, the approximative method is within 5% of the numerics for the separated mass-eigenstates and performs within 1% of the total momentum transfer cross-section for values of $d < 0.1a$. The approximation breaks down as $d \sim a$, where the upscattering cross-section is heavily suppressed due to the excited state energy being kinematically forbidden. We also note that in this region, the ground-state elastic cross-section receives a comparative boost before the numerics become difficult to calculate in the classical regime for $d \sim 9/10a$. As $d > a$, the total momentum transfer cross-section is determined totally by the ground-state process, as the upscattering results are purely imaginary.

As we will see in §6.2, the behaviour of the numerics as $d \gg a$ poses some serious issues for numeric calculations in this regime. An extension of the quasi-classical approximation [4] for inelastic processes, although not treated in this paper, would prove to be very valuable in examining this piece of parameter space.

6.2 $d \gg a$

As $d > a$, the numerics run into difficulties converging to an answer. Because the numerical methods require solving the Schrödinger equation up to large values of r and matching onto a superposition of Hankel functions, big issues arise when $d > a$. The root of these issues is that the second Hankel function asymptotically goes $\sim e^{-ikr}/r$, so for k purely imaginary,

the second column of the coefficient matrix C_ℓ^{ij} , blows up. We can see the effects of this on the dimensionless cross-section in Figure 6.

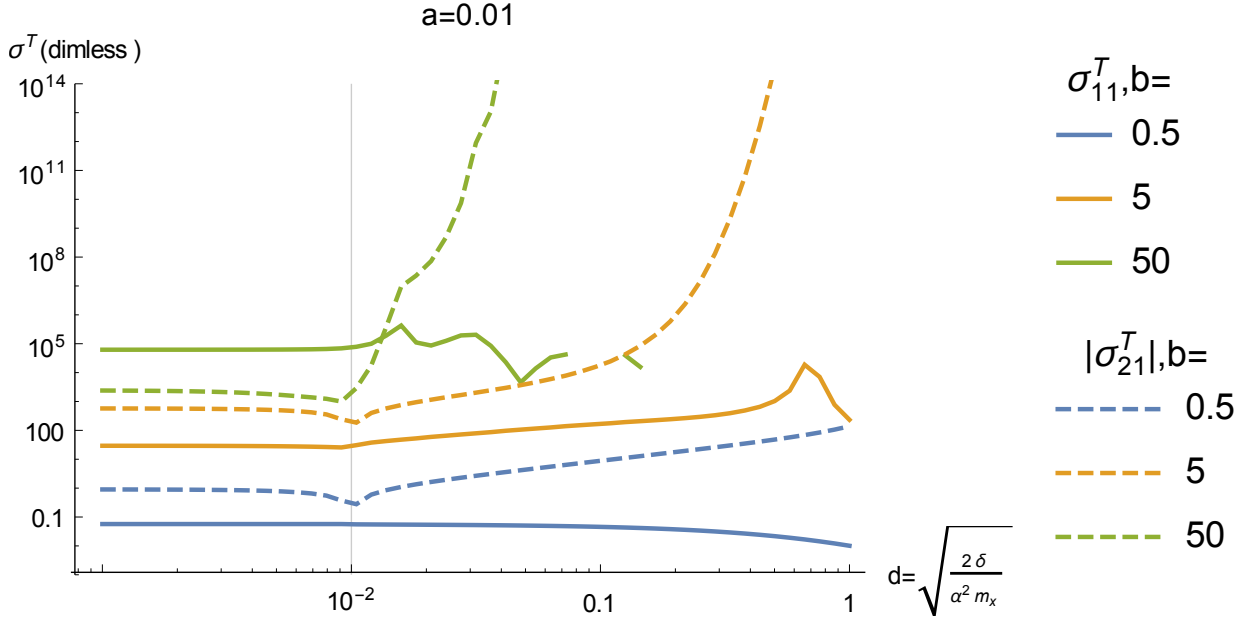


Figure 6: Transfer Cross-section for large d . (N.B. $\text{Re}[\sigma^{21}] = 0$ for $d > a$)

At values of $d \gtrsim 10a$, the purely imaginary upscattering term blows up, eventually becoming too large to be handled numerically. Fortunately, given that the only real scattering process in this regime is the $11 \rightarrow 11$ process, it is possible to derive the effective potential $V_{\text{box}}^{11}(r)$ from the relevant box diagram (Figure 1a), and calculate the cross-section using 1-state methods. This remains a point of interest for future research.

7 Analysis

With a toolkit of numerical and analytic methods, we can turn toward examining the phenomenology of inSIDious Matter. In what follows, we investigate first the effects of mass-splitting on the dark matter halo structure. This is done by calculating the total momentum transfer cross-section and comparing this to known restrictions from previous literature (Eq. (2)), and plotting its contours in (m_X, m_ϕ) -space in reference to the ground-state dark matter mass and the dark boson mass. After establishing the allowed parameter space from halo structure, we plot the total upscattering rate (weighted by $1/m_X$) in terms of the dark matter mass and the ratio between its mass and the dark boson mass. By doing this we make plain the apparent resonances. For all of the following analysis we take $\alpha = 0.01 \implies a_{dw} = 0.01$, and $a_{\text{cluster}} = 1/3$.

7.1 Subhalo Structure

Here we plot the dimensionful total momentum transfer cross-sections $\sigma_{11}^T/m_X + \sigma_{12}^T/m_X$ overlaid for values of d of differing $\mathcal{O}(a)$ on the dwarf scale. Included are central contours

at the required cross-section per DM mass, Eq. (2), as well as contours \pm a factor of 10.

Characterizing the increasing mass-splitting parameter d in Figure 7 is a subtle shifting of the peaks of the resonances. This is most visible on the first s-wave resonance, which is the resonance/anti-resonance pair furthest to the bottom-right of the plot (i.e. for small b , toward the perturbative regime). Most striking is the large-scale shifting of the allowed region in the Born region ($m_\phi/m_X \gg 1$). Due to the suppression of the upscattering term, the total transfer cross-section is comprised primarily of the ground-state elastic process, and the parameter space is significantly altered while retaining similar features near to the classical limit.

If we now push this feature as far as the numerics will currently allow and examine values of $d > a$, as we have done in Figure 8 the parameter space is further skewed from the purely elastic base case ($\delta = 0$). Here the momentum transfer cross-section is determined purely by the elastic process as the kinematically forbidden upscattering goes to zero. In the born limit, the tail of the plot has shifted noticeably. We see that the $|11\rangle \rightarrow |22\rangle$ process is strongly preferred in the Born limit, as this requires just one exchange as opposed to the 2-step $|11\rangle \rightarrow |22\rangle \rightarrow |11\rangle$ scattering. On the other end of the plot, near the classical limit, the contours have turned over, shifting toward the bottom left of the plot. Most striking is the movement of the resonances. Whereas Figure 7 saw the resonances mostly localized with slight shifts between the location of peaks, the larger mass-splitting has induced drastic shifts between resonant peaks, amplifying into the classical regime where the choice of d has considerable effect over which swath of parameter space is available.

7.2 Upscattering Rates

The natural next step in this analysis is to take the parameter space restrictions from §7.1 and plot the total upscattering rate accessible. In terms of the eventual decay of excited DM to visible γ -line emission, this will show the available total radiation parameter space. In order to cover a large amount of parameter space, for these contour plots, the upscattering contours are drawn with contours at $1000^n cm^2/g$. In these plots (Figure 10, Figure 11) it becomes clear that while the elastic and upscattering cross-sections share resonant peaks, the anti-resonances are offset, causing the total incoming ground-state transfer cross-section to have clear resonant peaks connected by smooth local minima. This has interesting consequences on what upscattering rates fit in the allowed parameter space, as the upscattering rate (σ_{21}) anti-resonances are not bounded by total transfer cross-section ($\sigma_{11}^T + \sigma_{21}^T$) anti-resonances.

7.2.1 Dwarf Scale

Here we examine the upscattering rates for a range of mass-splittings for dwarf spheroidal velocity halos. These halos are characterized by $a = v/\alpha \sim 0.01$ and we examine both small mass-splittings of $d = 10^{-3}a_{dw}$ in which there is negligible effect on halo structure, as well as the limiting cases of mass-splitting with $d = (0.1, 0.9, 0.99)a_{dw}$, where the lowest mass-splitting at which some noticeable change to the allowable parameter space from the transfer cross-section occurs for $d \sim 0.1a_{dw}$.

Figure 10 shows a rich variance to the parameter space over changes of the characteristic mass-splitting of the theory. We see in Figure 9a and Figure 9b that indeed for mass-

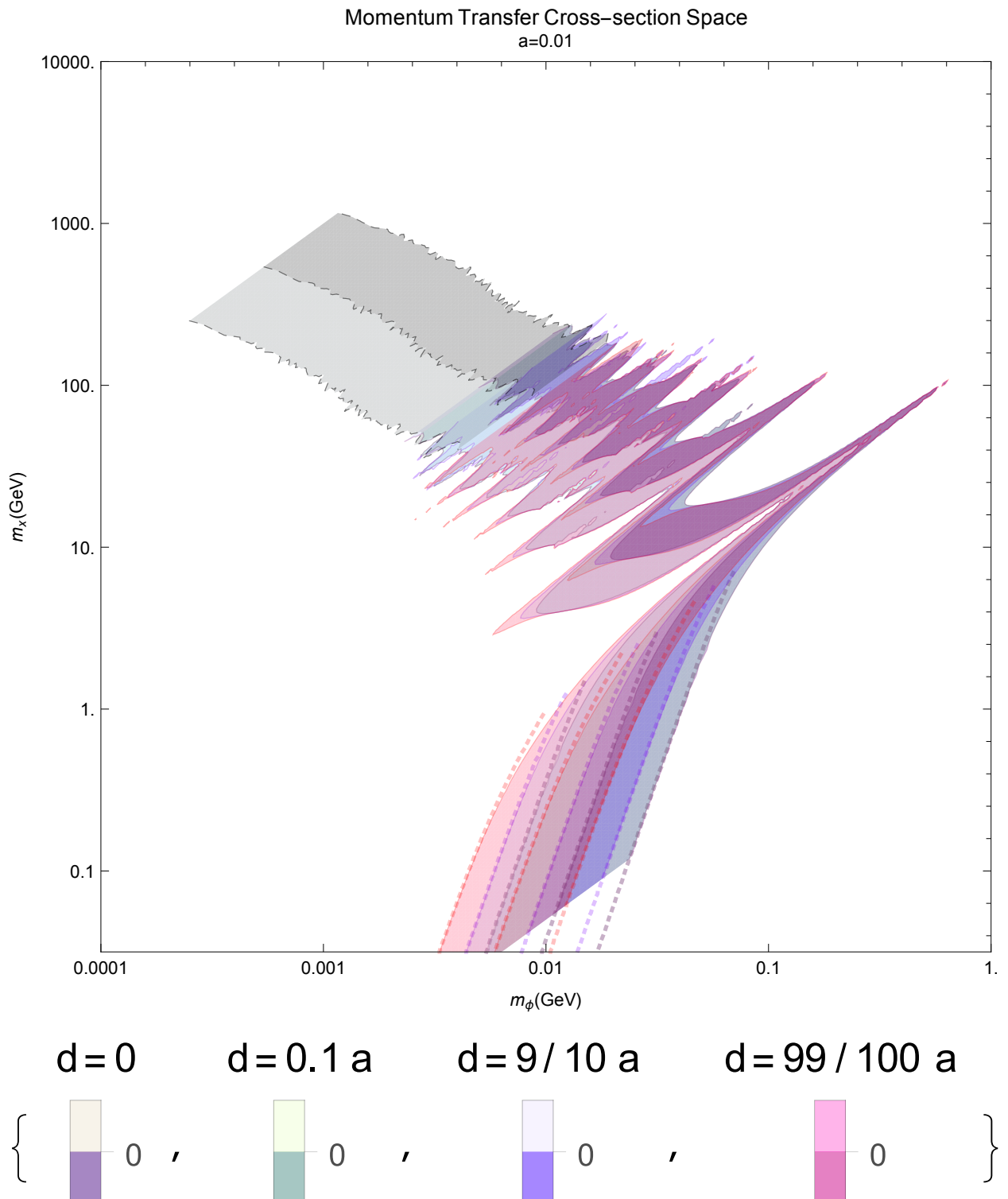


Figure 7: Momentum transfer cross-section σ_T/m_X contours for $d < a$. Values of constant b run in diagonals up and right, with b increasing up and left.

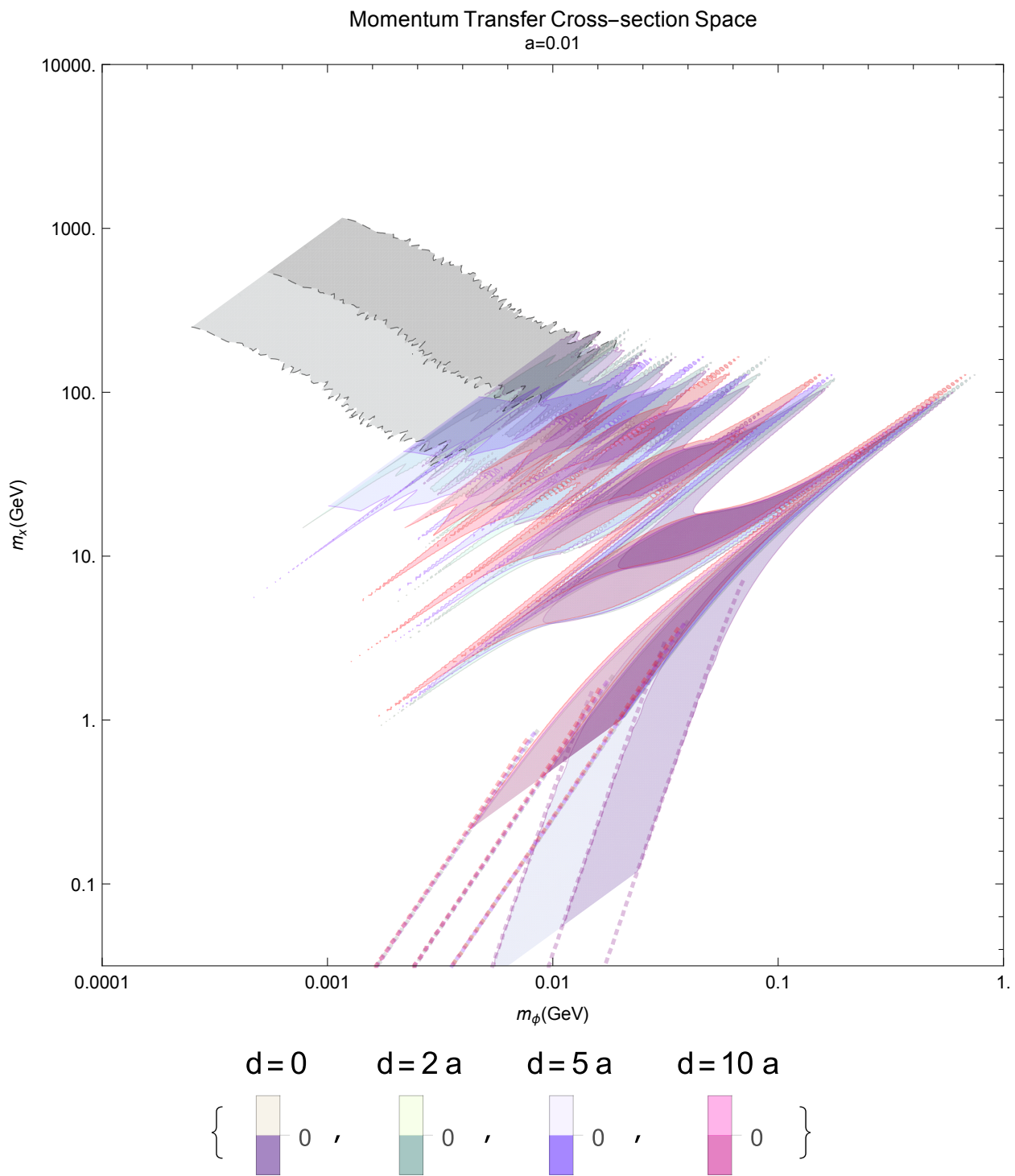


Figure 8: Momentum transfer cross-section σ_T/m_X contours for $d > a$.

Figure 9: Dwarf-scale Upscattering Rates σ/m_X

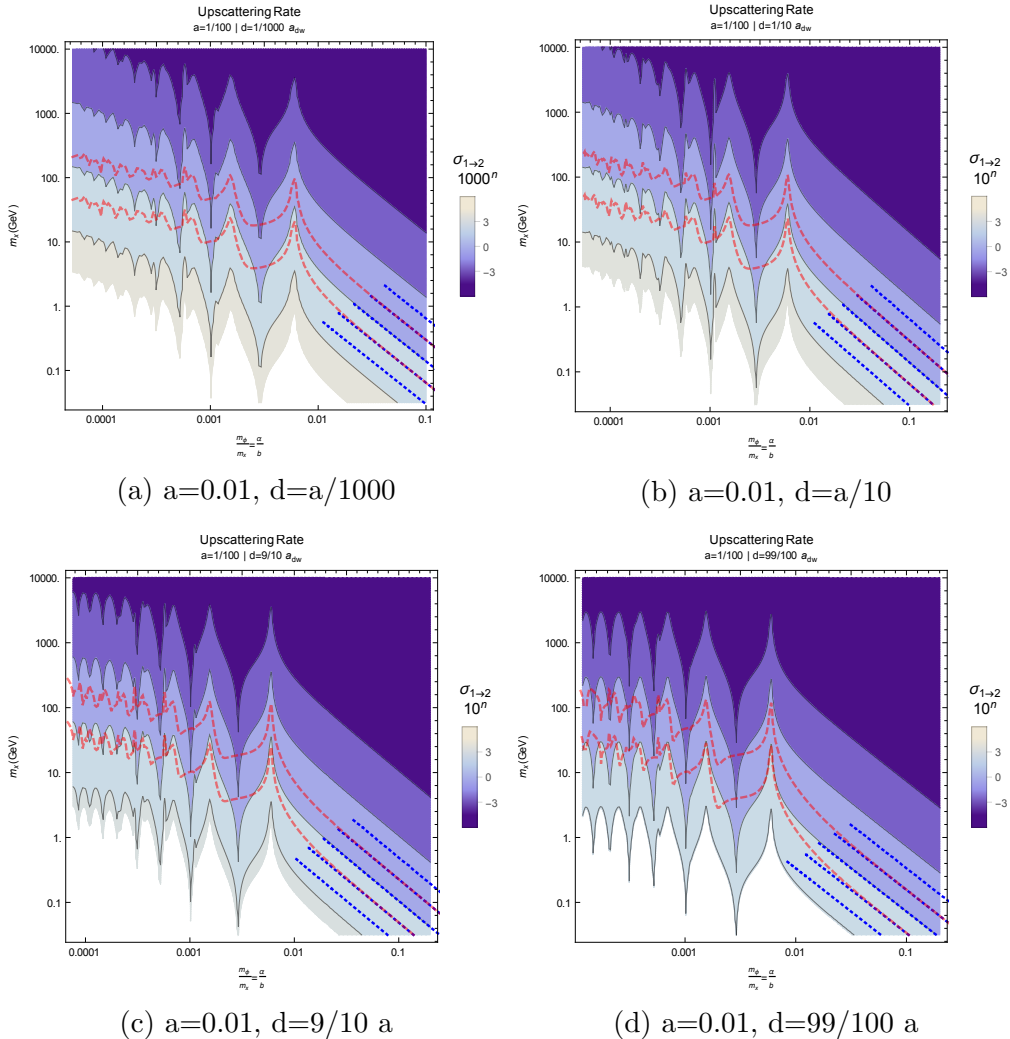


Figure 10: Upscattering Cross-sections ($\frac{\sigma^{21}}{m_X}$) with σ^T/m_X parameter spaces outlined in red and σ_{born}^T blue

splittings which are not within an order of magnitude of the characteristic kinetic energy of the galaxy, the parameter space remains largely unchanged, but that there remains a baseline for upscattering present even in the $\delta = 0$ case (although in that case it is meaningless to differentiate between the degenerate ground and excited states). Looking into the limiting cases in Figure 9c and Figure 9d, large-scale changes to the parameter space appear.

The allowed parameter space ranges over several orders of magnitude of upscattering rate, allowing for a considerable amount of “wiggle room” in obtaining a velocity-dependent upscattering cross-section that allows for the types of line emissions (such as the 3.56keV emission) that are visible only in cluster-scale objects.

7.2.2 Cluster Scale

It is also of some interest to examine the upscattering rates on a cluster scale for typical mass-splittings that are kinematically forbidden on a dwarf scale, even considering that the effect of a mass-splitting on the cluster transfer cross-section, and thus halo structure remains negligible for values below dwarf scale. Here the typical velocity of the cluster is well above that of a dwarf spheroidal, and so it is computationally easy to look at mass-splittings that would be troublesome at a dwarf scale. (Note that here we use a contour spacing at $\mathcal{O}(10)$)

For the most part there are no resonant features at the cluster scale for such a relatively small mass-splitting. Because of its high velocity the Born and classical regimes for cross-sections in Figure 11 are connected, effectively denying the formation of a resonant regime. This plot should, however, prove to be a reference point for the rates of γ -production available at a mass-splitting that gives rich dynamics to the available parameter space at a dwarf scale.

In particular this plot illuminates the importance of the classical regime in determining the parameter space, as the allowable region from the transfer cross-section (dotted) breaks from the upscattering rate near the classical limit and tracks across several orders of magnitude of upscattering rate for near constant DM mass. This further illuminates the importance of the development of quasi-classical methods that are accurate beyond $d \lesssim 10^{-1}a$, as suggested in §6.1.1.

7.3 3.56 keV mass-splitting

For the particular case of $\delta = 3.56\text{keV}$, we can utilize limits on the upscattering cross-section [3] taken from the analysis of xray line emissions on a cluster scale [2] to plot the available parameter space. The required value for the upscattering rate (and equivalently xray emission rate) is

$$\sigma_{21}^{\text{req'd}} = \left(\frac{10^{-19}\text{cm}^3/\text{s}}{v_{\text{cluster}}} \right) \times \left(\frac{m_X}{10\text{GeV}} \right)^2 \quad (45)$$

$$\frac{\sigma_{21}^{\text{req'd}}}{m_X^2} = 10^{-29} \left(\frac{\text{cm}}{\text{GeV}} \right)^2 \quad (46)$$

To plot the contours with this restriction we take a different approach to previous data generation as we require a constant δ and α_X . This means that each m_X corresponds to a

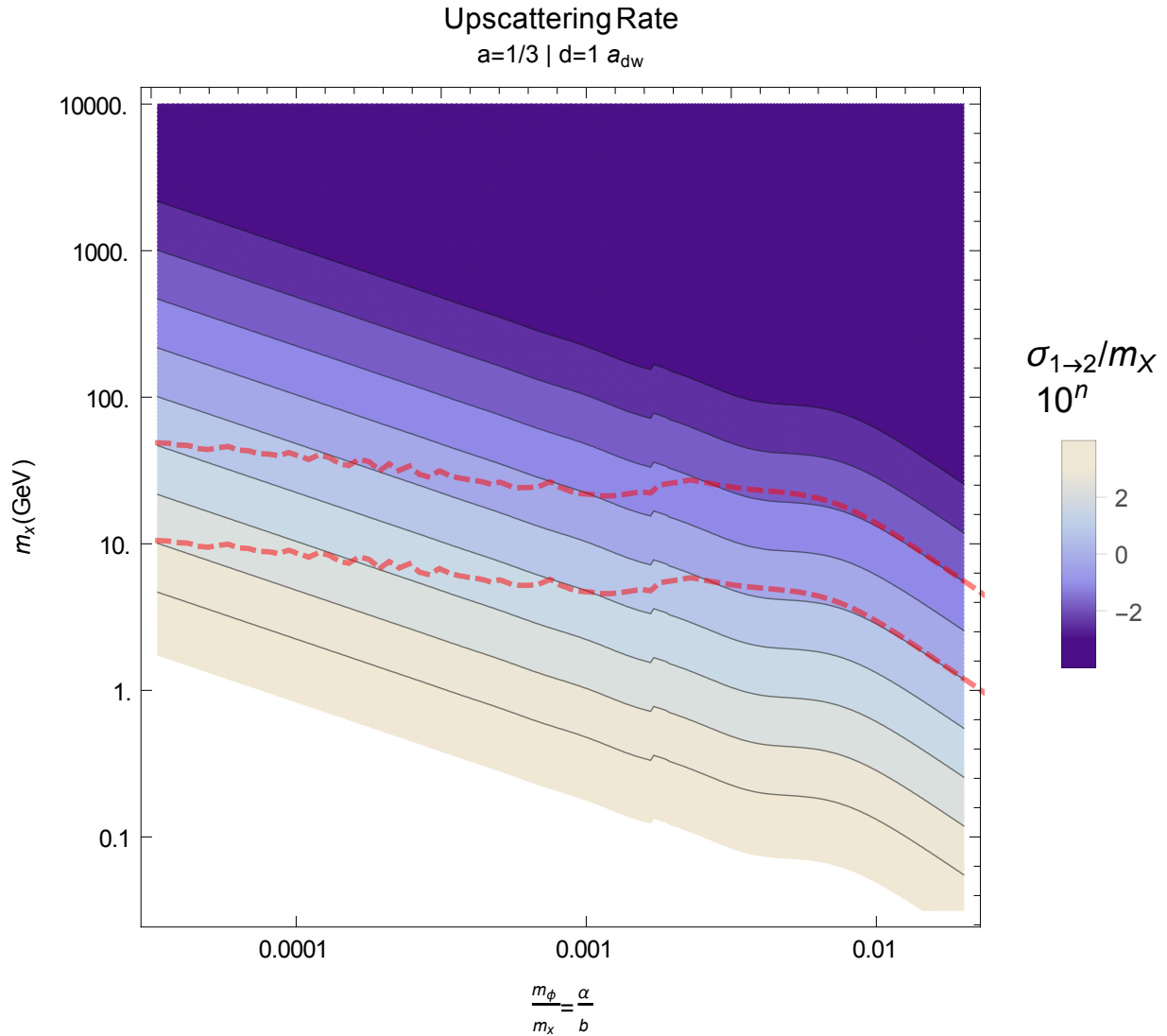


Figure 11: Cluster Up-scattering Cross-section: $a = a_{cl}$, $d = a_{dw}$, allowed parameter spaces outlined in red and σ_{born}^T blue. (N.B. results from σ_{class}^{21} are used for $b > 6$, causing the bump in the contours at that point)

particular value of $d = \sqrt{\frac{2\delta}{m_X \alpha^2}} = \sqrt{\frac{2(3.56)10^{-6}}{m_X(0.01)^2}}$. We calculate the dimensionless cross-section and draw contours at $(0.1, 1, 10) \times \sigma_{21}^{\text{req'd}} m_X^2$ in Figure 12 for a large swath of parameter space, well beyond previous results.

8 Conclusion

Throughout this paper we have developed a toolkit of numerical and analytic methods to facilitate the calculation of the characteristic particle physics quantities of an inSIDious Matter. This has allowed us to explore an expansive swath of the available parameter space allowed by a dark interaction force on the electro-magnetic scale ($\alpha_X = 0.01 \sim \alpha_{EM}$). In contrast to previous literature, we have pushed the limits of the numerical methods into the classical regime by considering a treatment beyond purely s-wave scattering. Our focus on the limiting region where increasing mass-splitting causes upscattering events to become kinematically forbidden has garnered very interesting results that suggest an even richer and more complex parameter space as we probe deeper.

A natural continuation of this inquiry would be to proceed in formulating from QFT the box potential for ground-state scattering of inSIDious Matter, thereby reducing the numerical difficulty from a 2-state problem to a 1-state problem for the region of interest. With the ability to finely probe the kinematically forbidden region, it will be possible to investigate the effects on dSph galaxies with upscattering turned off. These results can be compared against galactic cluster cross-sections that exhibit noticeable changes from a cluster-large mass-splitting, which can be treated effectively into the classical limit using the current methodology. For a complete treatment, it remains essential to develop a quasi-classical approximation of inSIDious Matter in order to fully explore the allowed parameter space.

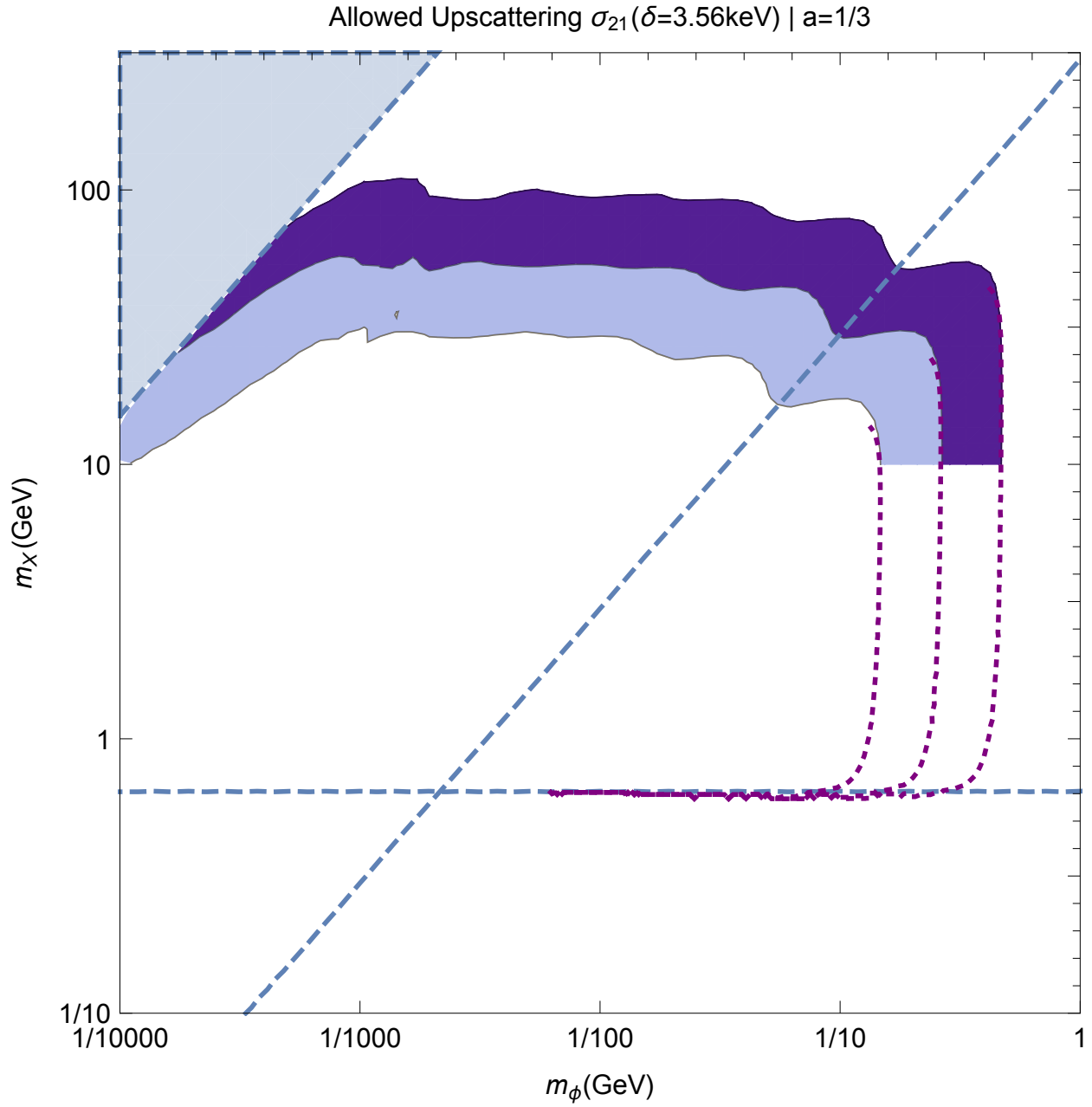


Figure 12: 3.56 keV mass-splitting parameter space: $a = a_{cl}$, $\delta = 3.56\text{keV}$
 Dashed lines mark: $(m_X \sim 1)$ kinematically forbidden region, $d > a$; $(\alpha_X m_X / m_\phi \sim 3)$ limit of previous results at classical limit ($ab = v m_X / m_\phi = 1$); $(\alpha_X m_X / m_\phi \sim 1500)$ current limit of calculations, above are higher ℓ -modes deeper into the classical regime

References

- [1] S. Tulin, H. B. Yu and K. M. Zurek, Phys. Rev. D 87, no. 11, 115007 (2013) [[arXiv:1302.3898 \[hep-ph\]](#)].
- [2] D. P. Finkbeiner and N. Weiner, (2014) [[arXiv:1402.6671 \[hep-ph\]](#)]
- [3] K. Schutz and T. R. Slatyer, (2014) [[arXiv:1409.2867 \[hep-ph\]](#)]
- [4] Landau, L., & Lifshitz, L. (1958). The Theory of Elastic Collisions. In Quantum mechanics, non-relativistic theory. London: Pergamon Press ;.
- [5] D. N. Spergel and P. J. Steinhardt, Phys. Rev. Lett. 84, 3760 (2000) [[astro-ph/9909386](#)].
- [6] S. Tulin, H. -B. Yu and K. M. Zurek, [arXiv:1210.0900 \[hep-ph\]](#).
- [7] Manoj Kaplinghat, Sean Tulin, Hai-Bo Yu (2015) [arXiv:1508.03339 \[astro-ph.CO\]](#)
- [8] S. W. Randall, M. Markevitch, D. Clowe, A. H. Gonzalez and M. Bradac, Astrophys. J. 679, 1173 (2008) [[arXiv:0704.0261 \[astro-ph\]](#)].
- [9] M. Vogelsberger, J. Zavala and A. Loeb, [arXiv:1201.5892 \[astro-ph.CO\]](#).
- [10] M. Rocha et al. [arXiv:1208.3025 \[astro-ph.CO\]](#).
- [11] J. Zavala, M. Vogelsberger and M. G. Walker, [arXiv:1211.6426 \[astro-ph.CO\]](#).
- [12] Esra Bulbul, Maxim Markevitch, Adam Foster, Randall K. Smith, Michael Loewenstein, et al. Detection of An Unidentified Emission Line in the Stacked X-ray spectrum of Galaxy Clusters. *Astrophys.J.*, 789:13, 2014.
- [13] Alexey Boyarsky, Oleg Ruchayskiy, Dmytro Iakubovskyi, and Jeroen Franse. An unidentified line in X-ray spectra of the Andromeda galaxy and Perseus galaxy cluster. 2014.
- [14] M. Boylan-Kolchin, J. S. Bullock and M. Kaplinghat, Mon. Not. Roy. Astron. Soc. 415, L40 (2011) [[arXiv:1103.0007 \[astro-ph.CO\]](#)].
- [15] M. Boylan-Kolchin, J. S. Bullock and M. Kaplinghat, Mon. Not. Roy. Astron. Soc. 422, 1203 (2012) [[arXiv:1111.2048 \[astro-ph.CO\]](#)].
- [16] A. A. Klypin, A. V. Kravtsov, O. Valenzuela and F. Prada, *Astrophys. J.* 522, 82 (1999) [[astro-ph/9901240](#)].
- [17] B. Moore, S. Ghigna, F. Governato, G. Lake, T. R. Quinn, J. Stadel and P. Tozzi, *Astrophys. J.* 524,L19 (1999) [[astro-ph/9907411](#)].
- [18] GKauffmann, S. D. M. White and B. Guiderdoni, Mon. Not. Roy. Astron. Soc. 264, 201 (1993).
- [19] J. S. Bullock, arXiv:1009.4505 [astro-ph.CO].

- [20] S. -H. Oh, W. J. G. de Blok, E. Brinks, F. Walter and R. C. Kennicutt, Jr, arXiv:1011.0899 [astro-ph.CO].
- [21] J. F. Navarro, C. S. Frenk and S. D. M. White, *Astrophys. J.* 490, 493 (1997) [astro-ph/9611107].
- [22] R. H. Wechsler, J. S. Bullock, J. R. Primack, A. V. Kravtsov and A. Dekel, *Astrophys. J.* 568, 52(2002) [astro-ph/0108151].
- [23] J. Dubinski and R. G. Carlberg, *Astrophys. J.* 378, 496 (1991).
- [24] R. A. Flores and J. R. Primack, *Astrophys. J.* 427, L1 (1994) [astro-ph/9402004].
- [25] J. D. Simon, A. D. Bolatto, A. Leroy, L. Blitz and E. L. Gates, *Astrophys. J.* 621, 757 (2005) [astro-ph/0412035].
- [26] R. K. de Naray and K. Spekkens, *Astrophys. J.* 741, L29 (2011) [arXiv:1109.1288 [astro-ph.CO]].
- [27] W. J. G. de Blok, S. S. McGaugh, A. Bosma and V. C. Rubin, *Astrophys. J.* 552, L23 (2001) [astro-ph/0103102].
- [28] L. E. Strigari, J. S. Bullock, M. Kaplinghat, J. Diemand, M. Kuhlen and P. Madau, *Astrophys. J.* 669, 676 (2007) [arXiv:0704.1817 [astro-ph]].
- [29] M. G. Walker, arXiv:1205.0311 [astro-ph.CO].
- [30] J. Knodlseder et al., *Astron. Astrophys.* 411, L457 (2003), astro-ph/0309442.
- [31] E. Churazov, R. Sunyaev, S. Sazonov, M. Revnivtsev, and D. Varshalovich, *Mon. Not. Roy. Astron. Soc.* 357, 1377 (2005), astro-ph/0411351.
- [32] J. Knodlseder, P. Jean, V. Lonjou, G. Weidenspointner, N. Guessoum, et al., *Astron. Astrophys.* 441, 513 (2005), astro-ph/0506026.
- [33] Tesla E. Jeltema, Stefano Profumo (2015) arXiv:1512.01239 [astro-ph.HE]